A Paradigm of Calendaring-Driven Electrode Microstructure for Balanced Battery Energy Density and Power Density

*Renming Zhan, Dongsheng Ren, Shiyu Liu, Zhengxu Chen, Xuerui Liu, Wenyu Wang, Lin Fu, Xiancheng Wang, Shuibin Tu, Yangtao Ou, Hanlong Ge, Andrew Jun Yao Wong, Zhi Wei Seh, Li Wang, and Yongming Sun**

R. Zhan, S. Liu, Z. Chen, X. Liu, W. Wang, L. Fu, X. Wang, S. Tu, Y. Ou, Y. Zhang, Prof. Y. Sun

Wuhan National Laboratory for Optoelectronics, Huazhong University of Science and Technology Wuhan 430074, China.

E-mail: yongmingsun@hust.edu.cn

A. J. Y. Wong, Z. W. Seh

Institute of Materials Research and Engineering, Agency for Science, Technology and Research (A*STAR), Singapore 138634, Singapore

D. Ren, L. Wang

Institute of Nuclear and New Energy Technology, Tsinghua University, Beijing 100084, China

Keywords: Compaction density, porosity, volumetric capacity, utilization, rate capability

Abstract: The microstructure of an electrode, which plays a critical role in the electrochemical performance of lithium-ion batteries, including the energy and power density, could be regulated by calendaring during electrode fabrication. For electrodes comprising of a given active material, binder, and conductive additive, porosity and tortuosity are the two key parameters that dictate ion diffusion. Due to compaction density affecting electron transport in the electrode, these parameters determine the volumetric capacity and specific capacity (active materials utilization) of an electrode under specific test conditions. We utilized calendaring to fabricate electrodes of different given thicknesses that shared the same mass loading but had different electrode parameters. Using a micrometer-scale Wadsley-Roth phase $TiNb_2O_7$ active material with intercalation chemistry, we investigated the relationship between electrochemical performances and electrode microstructures by both experimental investigation and theoretical modeling, providing a paradigm of calendaring-driven electrode microstructure for balanced battery energy density and power density. Along with the reduction in porosity, ion and electron

diffusion distance decreases, which is beneficial for charge transfer and rate capability. Nevertheless, the narrowed ion diffusion pathways would increase the resistance for ion diffusion. The rate capability, volumetric capacity, and materials utilization are thus predominantly restricted by the microstructures of the electrode. The dependence of electrochemical performance on the porosity and electrode compaction has been investigated to provide fundamental insights into the microstructures of electrodes for different application conditions. As an example, an optimized $TiNb_2O_7$ electrode with a compaction density of ~2.5 g cm^{-3} and mass loading of ~8.5 mg cm^{-2} provided the highest specific charge capacity of 271.3 mAh g^{-1} with high materials utilization of 63.2% and high capacity retention of 72.2% at 3 *C* in half cell configuration and 70.4% capacity retention at 6 *C* in full configuration. Also, a ~8 Ah level pouch cell with an optimized anode structure exhibited high capacity retention of 91.1% for 500 cycles at 0.5 *C*.

Lithium-ion batteries (LIBs) are the dominating power source for electric vehicles and electronics and have shown great promise in grid energy storage.[1-5] Energy density and power density are two of their most important parameters and should be well balanced for specific application conditions.[6-10] Herein, $TiNb_2O_7$ was employed as a model system to investigate their relationship due to the following considerations: As a typical Wadsley-Roth phase material with a monoclinic system (space group C2/m), $TiNb_2O_7$ possesses a stable Li^+ diffusion channel structure constructed by ReO_3-like regions (blocks) of corner- and edge-shared octahedra, and displays highly stable electrochemical lithium extraction/insertion behavior (Figure S1).[11-15] $TiNb_2O_7$ exhibits a comparable lithiation potential slope between 1–2 V (~1.5 V on average, *vs*. Li^+/Li) to $Li_4Ti_5O_{12}$, which is widely considered a good fast-charging battery anode (**Figure 1a**).[16-19] Also, it delivers a theoretical capacity of 387.6 mAh g^{-1}, which is over double that of $Li_4Ti_5O_{12}$ and slightly higher than mostly used graphite anode in comercial lithium ion batteries.[20-25] Specifically, the coupling of the reasonably high specific capacity and the high true density of $TiNb_2O_7$ (double that of graphite) suggests its potential practicability of realizing electrodes with high volumetric capacity and batteries with high volumetric energy density (Figure 1b). The theoretical volumetric capacity of the $TiNb_2O_7$ anode reaches 1683.92 mAh cm^{-3}, far exceeding graphite at 818.4 mAh cm^{-3} and $Li_4Ti_5O_{12}$ at 600.25 mAh cm^{-3} (Figure 1c). Also, the as-resulted reduced electrode thickness with the same areal capacity as other electrodes provides feasibility to speed up the electrochemical reaction at the electrode level and realize high rate capability.

Besides materials choice and design, the microstructure of an electrode plays a critical role in the energy (volumetric and gravimetric) and power density of lithium-ion batteries, as well as cycling life, which is often ignored in academic research.[26-29] The porosity, compaction density, thickness and mass loading are the main parameters for electrodes with given active materials, binder and conductive additive, as well as electrode conductivity and electrode resistivity, which together can show the characteristics of electrode microstructures. Numerical modeling was employed to study/simulate the overall electrochemical performance of lithium-ion batteries,[30-33] and electrochemical performance using $LiNi_{1/3}Co_{1/3}Mn_{1/3}O_2$ and $LiFePO_4$ electrodes with different electrode thicknesses was investigated.[34] However, the effect of electrode microstructures on electrochemical performance remained unrevealed. In practical electrodes, one needs to take into consideration the compaction density (*D*c, which is highly related to the morphology and particle size of active materials) during the calculation of volumetric energy density, which was measured as ~1.5 g cm^{-3}, ~1.3 g cm^{-3}, and ~2.8 g cm^{-3} for commercial graphite, $Li_4Ti_5O_{12}$ and fabricated $TiNb_2O_7$, respectively. Micrometer scale $TiNb_2O_7$ active particles were used to maximize the high volumetric capacity (Figure S2). Although the value of the true density of $Li_4Ti_5O_{12}$ is much higher than that of graphite, the compaction density values are similar. This is because commercial $Li_4Ti_5O_{12}$ active materials are often in the nanoscale, while the size of graphite particles reaches several micrometers, which leads to denser compaction of the graphite electrode with lower porosity (*P*). As such, $TiNb_2O_7$ could be a promising anode material for fast-charging/discharging batteries due to its significant advantage in safe working potential and reasonably high volumetric/specific capacity.

Due to the safety concerns caused by the low lithiation potential of graphite, we focused on comparing the volumetric energy density of cells using $Li_4Ti_5O_{12}$ and $TiNb_2O_7$ anodes. Considering the volume of all the battery components, the volumetric ratio of the negative electrode of a 10 Ah-level $LiFePO_4$ battery would be reduced from 55.4% to 26.9% when replacing $Li_4Ti_5O_{12}$ with $TiNb_2O_7$ (Table S1, S2, and Figure S3,). Thus, the corresponding volumetric energy density of the battery increases from 182 Wh L^{-1} to 292 Wh L^{-1} (Figure 1d). Due to the increase in compaction density and specific capacity, and decrease in the electrolyte absorption due to lower porosity, the specific energy density of $TiNb_2O_7$-based batteries also far outperforms the $Li_4Ti_5O_{15}$-based batteries.[35-38] The above analysis supports the distinct advantage of $TiNb_2O_7$ over graphite and $Li_4Ti_5O_{15}$ with respect to both the safe working potential and practical high volumetric capacity, as well as rate capability.

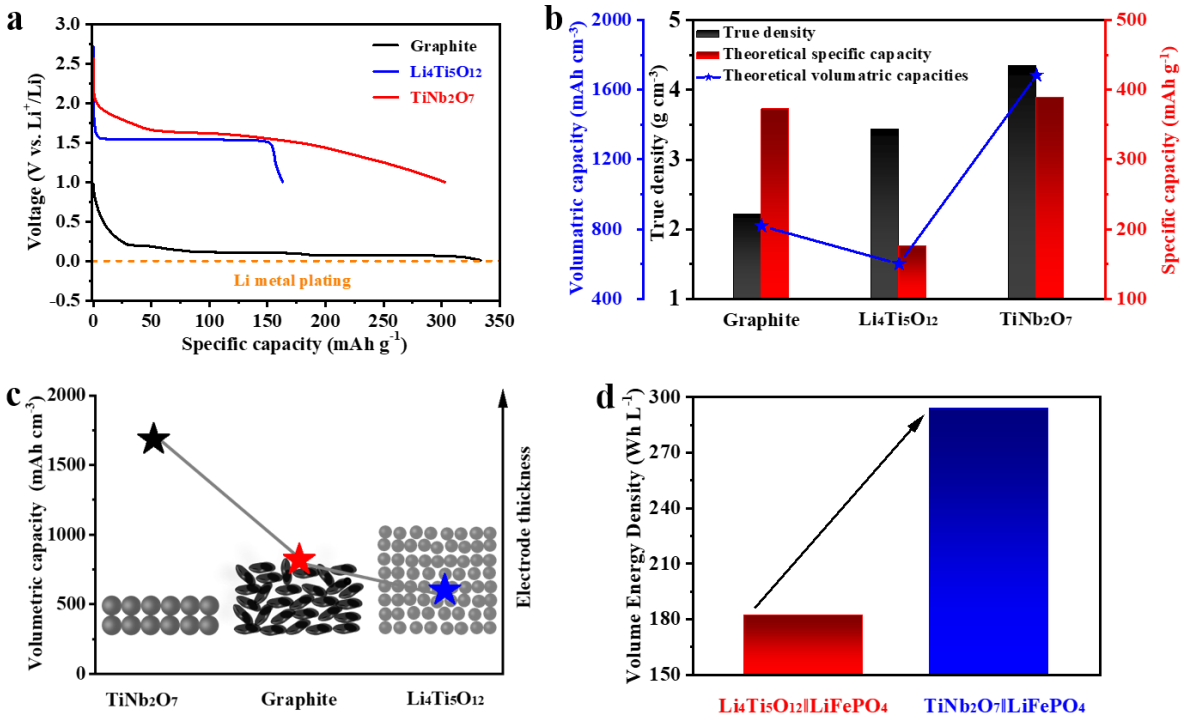

Figure 1. (a) Lithiation potential and specific capacity for $Li_4Ti_5O_{12}$, graphite, and $TiNb_2O_7$. (b) The comparison of the true density, specific capacity, and volumetric capacity of $Li_4Ti_5O_{12}$, graphite, and $TiNb_2O_7$. (c) Effect of electrode thickness on the volumetric capacity of $Li_4Ti_5O_{12}$, graphite, and $TiNb_2O_7$. (d) The volumetric energy density of 10 Ah-level $LiFePO_4$ ‖ $TiNb_2O_7$ and $LiFePO_4$ ‖ $Li_4Ti_5O_{12}$ cells.

During the practical fabrication of electrodes, compaction density (porosity) should be considered to optimize their electrochemical performance. Although electrodes with high compaction densities would result in low porosity and thus low take-in of electrolyte, leading to electrodes with high volumetric capacity and batteries with high energy densities, on the other hand, reasonable porosity is beneficial for charge transport, which is beneficial for realizing electrodes with high rate capabilities and batteries with high power densities. Therefore, it is highly desirable to investigate the relationship between the compaction density (porosity) and the electrochemical performance of electrodes, which remains a basic principle of battery design for various applications. Herein, $TiNb_2O_7$ electrodes were fabricated, which consisted of 90 wt% active material, 7 wt% super P conductive additive, and 3 wt% hybrid binder (carboxy methylcellulose: styrene-butadiene rubber = 1:1 in weight). Then, electrodes of decreasing thicknesses of ~55 μm, ~41 μm, ~37 μm, ~34 μm to ~30 μm were obtained via calendaring by tuning the interval distances of rollers (**Figure 2**a, Figure S4, and S5). All the electrodes had a mass loading of ~8.5 mg cm^{-2} and were labeled S1 to S5, respectively. Accordingly, the values of compaction density are 1.5 g cm^{-3}, 2.1 g cm^{-3}, 2.3 g cm^{-3}, 2.5 g cm^{-}

^{3} and 2.8 g cm^{-3} for these electrodes (Figure 2c). With the increase in compaction density, the values of porosity of the samples S1 to S5 decreased to 61%, 46%, 41%, 36%, and 28%, and they were calculated according to the following equation:[37]

$$P = (1-\frac{Dc}{D_0})*100\% \quad (1)$$

Where D_0 is the average density for all the materials of the electrode, and D_0 is calculated as the following equation:

$$D_0=\frac{1}{Da + Db + Ds} \quad (2)$$

Where Da is the ratio of the mass fraction of the active material in the electrode to the true density of the active material; Db is the ratio of the mass fraction of the binder in the electrode to the true density of the binder; Ds is the ratio of the mass fraction of the conductive agent in the electrode to the true density of the conductive agent.

Based on the results of the discussion above, the structures of these electrodes are illustrated in Figure 2b. For electrodes with high porosity, there exists an abundance of pores between active materials and conductive additives in electrodes, creating a discontinuous electronic conductive network. This situation changes gradually with the reduction of porosity.[27] At the lowest porosity of 28% for the S5 electrode, an interconnected electronic transport network could form, allowing the electrode to realize high materials utilization and high rate capability. However, the decrease in porosity directly narrows the transport pathways of Li^+ ions, which would hamper their diffusion and further deteriorate the rate capability of electrodes.[39, 40] Thus, for practical electrode design, the balance between transportation of Li^+ ions and electrons should be considered by adjusting compaction density (porosity) to optimize their electrochemical performance with respect to rate capability and specific capacity. The volumetric capacity of the electrodes then regulated by the compaction density and specific capacity. Electrode structures should be optimized to meet the demand for different applications. For example, high energy density batteries call for high compaction density electrodes due to fast ionic transport in the electrode not being the priority during electrode design and fabrication.[38]

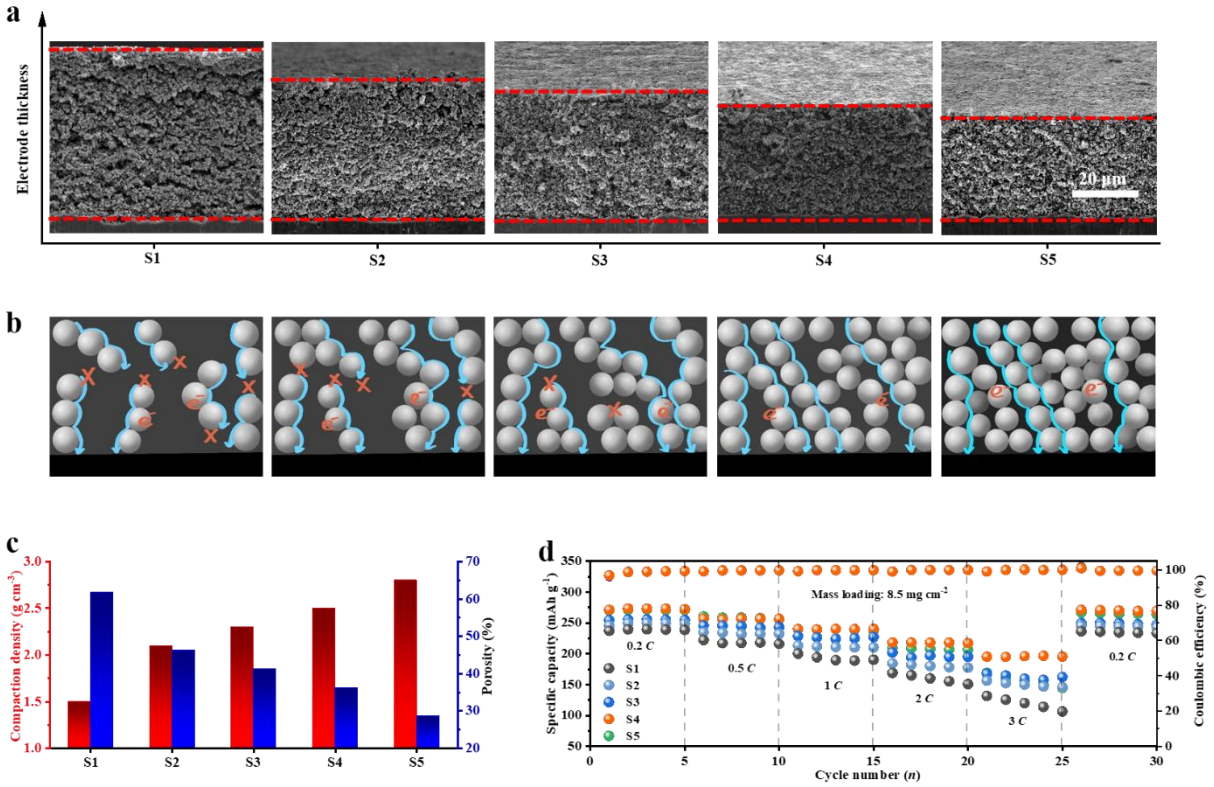

Figure 2. (a) Cross-section SEM images of $TiNb_2O_7$ electrodes with different compaction densities (S1-S5). (b) Illustration of microstructures for the S1-S5 electrodes. (c) The comparison of the compaction density, porosity and (d) rate performance for the S1-S5 electrodes.

These as-fabricated electrodes were then subjected to electrochemical charge/discharge cycling at various *C* rates to investigate the effect of compaction density (porosity) on the utilization ratio of active materials under various test conditions. As shown in Figure 2d, it was observed that the electrodes with the same mass loading (~8.5 mg cm^{-2}) but different compaction densities displayed different reversible specific capacities at 0.2 *C*. With a low compaction density of 1.5 g cm^{-3}, the reversible capacity of the electrode (S1) was 237.1 mAh g^{-1}, gradually increasing to 245.7, 254.7, and 271.3 mAh g^{-1} for the electrodes with compaction densities of 2.1, 2.3, and 2.5 g cm^{-3} (S2 to S4), respectively. Further increasing the compaction density to 2.8 g cm^{-3}, the electrode (S5) delivered a similar capacity (270.4 mAh g^{-1}) to S4, showing the maximized capacity for these specific electrodes with the same mass loading and different compaction densities. Correspondingly, Figure S6a showed the voltage-capacity plots of the S1-S5 electrodes at 0.2 *C*, where the S4 and S5 electrodes displayed the smallest voltage hysteresis of 0.042 V compared to 0.114 V for the S1 electrode (Figure S7a). Together with their highest specific capacities among the electrodes with different compaction densities, the highest volumetric capacity and energy efficiency could be expected. The same trend in

capacity comparison and voltage hysteresis for the S1 to S5 electrodes were observed when different current densities of 0.5, and 1 *C* were used (Figure S6b, c and Figure S7b, c). The difference in reversible capacities and voltage hysteresis of these electrodes are highly related to the integrity of the electron transport network in electrodes. In electrode S1, due to the loose structure, the conductive additive could not form an interconnected network, resulting in the electrons being unable to be freely transported throughout the electrode and a decrease in active material utilization. Accompanied by the increase in compaction densities, better connections between active particles and conductive additives were realized, and thus more electron transport pathways were formed. As such, the electrodes (S2 to S4) exhibited increased reversible capacity because of higher active material utilization. The S5 electrode exhibited a similar capacity to the S4 electrode without any increase in capacity, suggesting the upper limit of active materials utilization. Under high current densities (e.g., 2 and 3 *C*), the rules for reversible capacity comparison change (Figure S6d, e). The S4 electrode delivered the highest capacity of 196.1 mAh g^{-1} at 3 *C*, much higher than 159.9 mAh g^{-1} for the S5 electrode. Also, it is observed that the S4 electrode delivered the smallest voltage hysteresis of 0.116 V and 0.29 V in contrast to 0.194 V and 0.329 V for the S5 electrode at the 2 and 3 *C* current density (Figures S7d and e). This might be because the control step for reversible capacity in the electrode turns from electronic transport to ionic transport under high current density. The low porosity (high compaction density) of the S5 electrode possessed less ionic transport pathways and large diffusion impedance, which was not beneficial for fast ionic transport. In our experiment, for a TNO electrode with 3 wt% binder and 7 wt% conductive additive, an active mass loading of ~8.5 g cm^{-3} and a compaction density of 2.5 g cm^{-3} was ideal with respect to rate capability, specific capacity, and energy density. It is noted that the S4 electrode with a high active mass loading delivered a high reversible capacity of 216.1 mAh g^{-1} at 1 *C* after 100 cycles for 89% capacity retention, indicating good cycling stability (Figure S8). Additionally, regardless of the capacities obtained at 3 *C*, the capacities could be recovered when the test current density was reverted to 0.2 *C*, showing the good stability of all the electrodes.

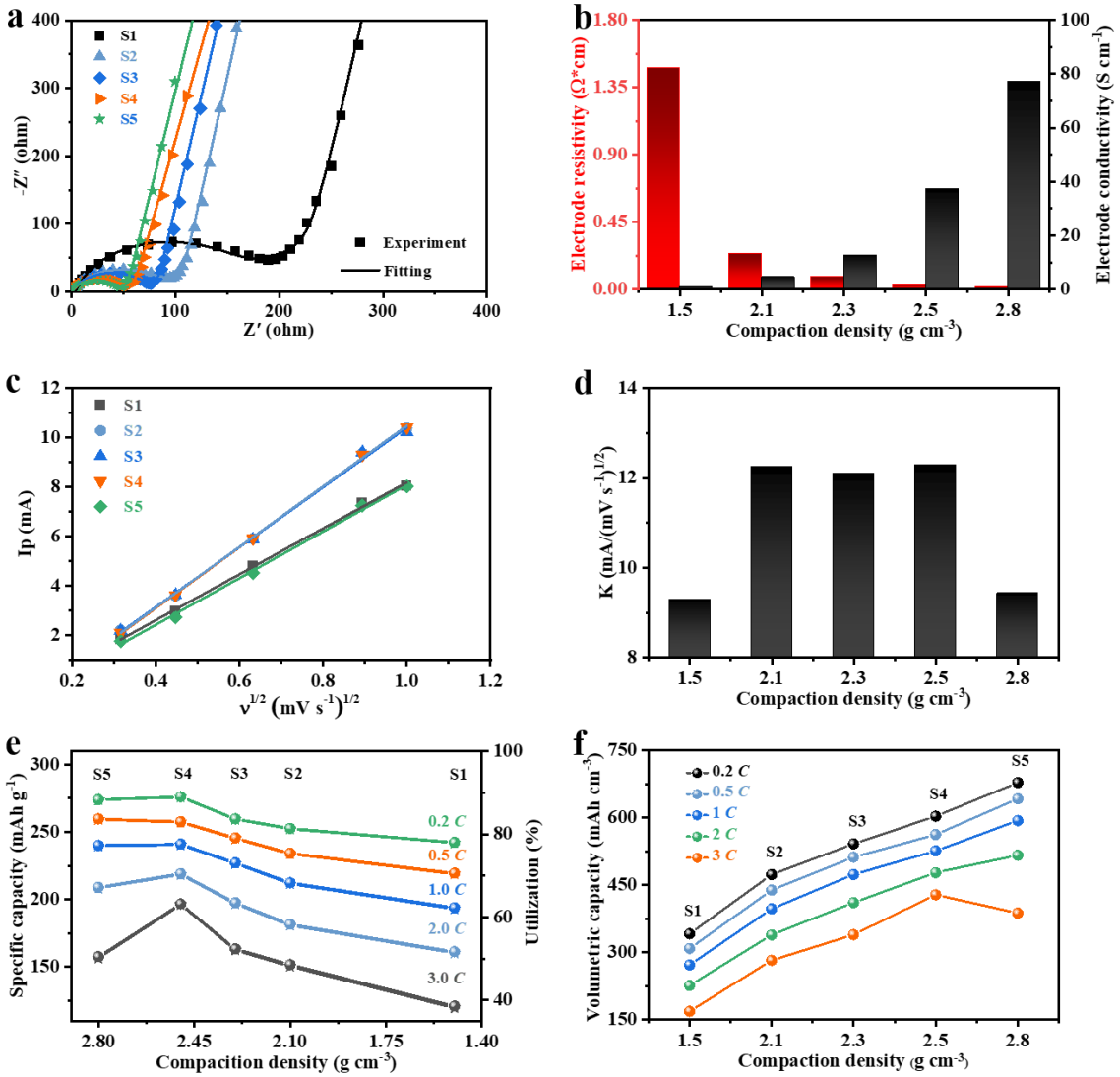

Figure 3. (a) Electrochemical impedance spectra and the corresponding fitting results of the S1-S5 electrodes at the same state of charge. (b) Resistivity and conductivity of electrodes (S1 to S5) with different compaction densities. (c) Presentation of the linear relationship between the cathodic peak current (Ip) and the square root of the scan rate ($v^{1/2}$) of the S1-S5 electrodes (d) and the corresponding slope values. (e) The relationship of active materials utilization of the S1-S5 electrodes at different current densities. (f) The relationship of volumetric capacity of the S1-S5 electrodes at different current densities.

Electrochemical impedance measurement was conducted at the same state of charge of the electrodes to reveal the mechanism behind the different capacities and rate capabilities of the S1-S5 electrodes (**Figure 3**a). The corresponding electron transfer resistance was fitted according to the equivalent circuit shown in Figure S9. The value gradually decreased from 150 Ω to 66 Ω for the S1-S3 electrode with the increase in compaction density, and it remained low and stable (45 Ω and 40 Ω for S4 and S5 electrodes, respectively) when the compaction density further increased. In addition, the resistivity and conductivity of electrodes (S1-S5) were

measured directly by a four-probe instrument (Figure 3b). The values of electrode resistivity rapidly decreased from 1.48 to 0.081 Ω·cm for the S1-S3 electrodes, and the S4 and S5 electrodes exhibited very close resistivity values of 0.027 Ω·cm and 0.013 Ω·cm, respectively. Correspondingly, small values of electrode conductivity were shown for electrodes with relatively low compaction density (0.67 S cm^{-1}, 4.29 S $cm^{-1}$and 12.35 S $cm^{-1}$for the S1, S2, and S3 electrodes, respectively), and the S4 and S5 electrodes with relatively high compaction density displayed large values of electrode conductivity of 37.04 S cm^{-1} and 76.92 S cm^{-1}, respectively. The above results indicated that a well-established electronic conductive network was formed in the S4 and S5 electrodes. Note that the decrease of resistivity from the S4 to S5 electrode was very low, suggesting that any further increase in compaction density beyond 2.5 g cm^{-3} (S4) would not cause a decrease in resistivity or an increase in the conductivity of the electrodes. Over-compaction of electrodes leads to a reduction in porosity, narrowing the pathways and increasing the resistance for the lithium-ion diffusion. Cyclic voltammetry (CV) curves of the S1-S5 electrodes at different scan rates were used to estimate the corresponding lithium-ion diffusion capability (Figure S10). A linear relationship between the anodic peak current (Ip) of the S1-S5 electrodes and the square root of the scan rate was verified, indicating diffusion-controlled lithium transport behavior in the electrodes (Figure 3c). The corresponding slope was calculated (noted as *k*), and its plots with compaction density for different electrodes were recorded in Figure 3d, where k^2 was directly proportional to the Li^+ diffusion coefficient (D). Their relationship is shown by the following formula:

$$i_P = 2.69\times10^5 An^{3/2}C_0D^{1/2}v^{1/2} \quad (3)$$

In this formula, the surface area (A), charge transfer number (n) and molar concentration of Li^+ (C_0) in these electrodes are constant. The Li^+ diffusion coefficient (D) of the as-measured electrodes can be directly compared by the ratio of peak current (I_P) and scan rate (v).[41] With given mass loading of electrodes, low compaction density would lead to high electrode porosity but long Li^+ diffusion distance due to the increase of electrode thickness, the former of which is beneficial for Li diffusion and the latter is detrimental. The largest electrode thickness (55 μm) and maximized concentration polarization of the S1 electrode (discussed latter, Figure 4c) explained the low slope value for the linear relationship between the peak current and the square root of the scan rate. The results showed that the S2-S4 electrodes with compaction densities of 2.1, 2.3, and 2.5 g cm^{-3} shared a similar fast Li^+ diffusion capability. The shorter diffusion pathways (by reduced electrode thickness) benefitted the Li^+ diffusion, which offset the increase in resistance caused by lower porosity. Such results bring an overall increase in energy density without sacrificing the rate capability of the S4 electrode, thus optimizing the overall

electrochemical performance. This analysis supports the slight increase in specific capacity and active material utilization at a low current density of 0.2 *C* from the S1 to S5 electrode. When the current density is increased to 3 *C*, the S4 electrode delivered the highest specific capacity of 196 mAh g^{-1} and materials utilization of 63.2%, which was 1.64 times that of the S1 electrode (Figure 3e). The plots of volumetric capacity *vs*. compaction density showed a continuous increase of volumetric capacity with the increase of compaction density from 1.5 to 2.8 g cm^{-3} when tested under 0.2 to 2 *C*. The S4 electrode showed a peak volumetric capacity of 428.4 mAh cm^{-3} under 3 C, in accordance with the result of materials utilization (Figure 3f). The compaction density and porosity of the S4 electrode addressed the trade-off between active materials utilization and volumetric capacity in the as-used electrode, which could be generalized to other electrode systems. The idea of compaction density regulation is straightforward to maximize the utilization of active materials and improve the energy density of batteries at specific current conditions. Other test conditions, such as temperature, would also significantly affect the electrochemical behavior of electrodes, which should also be considered during electrode fabrication.

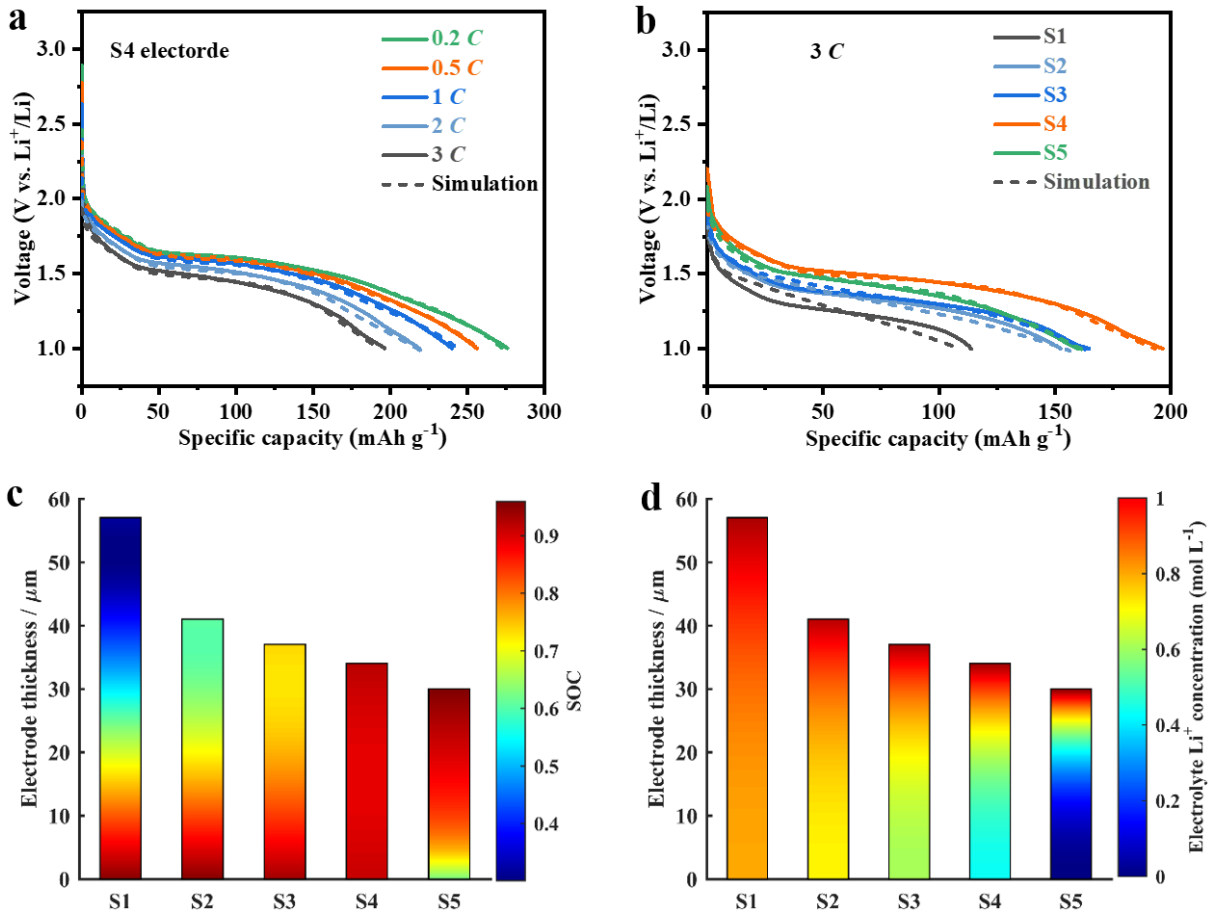

Figure 4 COMSOL Multiphysics (ver5.4) simulate results. (a) Voltage-capacity plots of the S4 electrode at different C-rates (0.2, 0.5, 1, 2 and 3 *C*). (b) Voltage-capacity plots of the S1-S5

electrodes at 3 *C*. Distribution of Li^+ concentration in (c) $TiNb_2O_7$ and (d) electrolyte at the end of the charged state at 3 *C*.

An electrochemical model was built in COMSOL Multiphysics (ver5.4) based on Newman's P2D (porous two dimensional) model[42] to simulate the electrochemical performance of different compaction density $TiNb_2O_7$ electrodes (S1-S5), with the governing equations listed in Table S3 and the physical variables in Table S4.The related physio-electrochemical parameters used in the electrochemical model are listed in Table S5. The model was validated by comparing the voltage-capacity plots of the S1-S5 electrodes at different *C*-rates, as shown in Figures 4a and b. The simulation results agreed well with the experimental results, indicating the excellent accuracy of the proposed model. Based on the validated model, the distributions of Li concentration in solid and electrolyte phase at the end of the charged state at 3 *C* were presented in Figures 4c and d to reveal the root cause of the differences in discharge capacity between S1-S5 electrodes. As shown in Figure 4c, electrode S1 which had a low compaction density of 1.5 g cm^{-3}, exhibited a large SOC gradient in the solid phase, leading to a low utilization ratio of active materials. Only $TiNb_2O_7$ materials near the current collector reach a high SOC (>0.9), while those near the separator are less lithiated (SOC<0.4), mainly due to the low electrode conductivity inside electrode S1. With the increase of compaction density from 1.5 g cm^{-3} (S1) to 2.5 g cm^{-3} (S4), the SOC gradient in the electrode phase decreased, with the S4 electrode presenting a homogeneous Li^+ distribution and thus delivering the highest specific capacity under 3 *C*. As the compaction density further increases to 2.8 g cm^{-3} (S5), Li^+ transport in the electrolyte became the rate-determining step under 3 *C*. As shown in Figure 4d, a large Li gradient in the electrolyte was observed in electrode S5, and a 14 μm Li^+ depletion layer (c_{Li+} < 0.2 mol L^{-1}) appeared near the current collector due to the reduced transport pathway. That led to insufficient lithiation (SOC < 0.8) of the active materials near the current collector and deteriorated utilization of active materials in the S5 electrode. Besides simulations on the $TiNb_2O_7$ electrodes with mass loading of 8.5 mg cm^{-2}, investigation on electrodes with lower (5 mg cm^{-2}) and higher (12 mg cm^{-2}) mass loadings were further conducted. As shown in Figure S11, the electrode with low mass loading showed only slight increase of specific capacity with the increase of compaction density, and both of the electrode and electrolyte exhibited uniform Li^+ distributions at the end of charged state at 3 *C* (Figure S12a, b), benefiting from the shortened transport distances of Li^+ and electron. In contrast, the compaction density had significant influence on the electrochemical performance of the high mass loading $TiNb_2O_7$ electrodes. As shown in Figure S11, the optimal compaction density of the high mass loading electrode shifted to a lower value compared to that of the medium (8.5

mg cm^{-2}) mass loading electrode. The high-mass-loading $TiNb_2O_7$ electrode showed severe capacity losses under low (1.5 g cm^{-3}) and high (2.8 g cm^{-3}) compaction density, due to the extremely heterogeneous distribution of Li^+ in the $TiNb_2O_7$ electrode and electrolyte (Figure S12c, d). The results indicate that compaction density plays a more important role in the electrochemical performance of high mass loading electrodes, and thus should be regulated seriously.

To investigate the electrochemical performance of the as-fabricated $TiNb_2O_7$ electrodes, coin cell-type full cells consisting of $LiFePO_4$ cathode (commercially for fast-charging batteries) and optimized $TiNb_2O_7$ anode (S4) were assembled with cathode active mass loading of ~12.7 mg cm^{-2} and measured under different current densities (**Figure 5**a-c). At 0.2 *C*, the full cell exhibited a high reversible discharge capacity of 139.7 mAh g^{-1} (calculation through all the positive electrode loading) and an areal capacity of 1.78 mAh cm^{-2}. The values showed only a slight decrease with the increase of *C* rates and capacity retention. Satisfyingly, a high specific capacity of 98.3 mAh g^{-1} and an areal capacity of 1.25 mAh cm^{-2} were realized at the charge/discharge rate of 6 *C*, and the corresponding capacity retention was 70.4%, showing the great potential of the porosity-compaction balanced $TiNb_2O_7$ in high-power lithium-ion batteries. The voltage-capacity curves displayed only slight increases in overpotential with the increase of *C* rates (Figure 5c), indicating the optimized electrode porosity for the maximization of the rate capability. Long-term cycling measurement was further conducted at 2 *C*. With an initial discharge capacity of 120.9 mAh g^{-1}, impressive capacity retention of 84.6% was realized for 500 cycles (Figure S13). This promising electrochemical data inspired us to explore the practical application of $TiNb_2O_7$ anode with optimized electrode design with full pouch cell configuration (Figure 5d, e). Double-sided $TiNb_2O_7$ electrode with active mass loading of ~20 mg cm^{-2} was fabricated as the anode and double-sided $LiFePO_4$ with a mass loading of ~35 mg cm^{-2} was used as the cathode. Surprisingly, the pouch cell delivered a high reversible capacity of ~8 Ah at 0.5 *C* and displayed high capacity retention of 91.1% after 500 cycles (Figure 5f, g, and Figure S14). Such results verified the successful fabrication of $TiNb_2O_7$ electrode with well-balanced electrode construction that supported the long-term cycling of full batteries at reasonable C rates. A 1Ah-level $LiFePO_4$||$TiNb_2O_7$ pouch cell was assembled to further test the *C*-rate performance. As shown in the Figure 5h and i, the cell exhibited a high reversible discharge capacity of 0.812 Ah at 6 C, delivering a high capacity retention of 74.7% based on the capacity at 0.2 *C*. Also, only slight increase in potential hysteresis was observed in the charge/discharge curves of the cell at 6 *C* in comparison to that at 0.2 *C*.

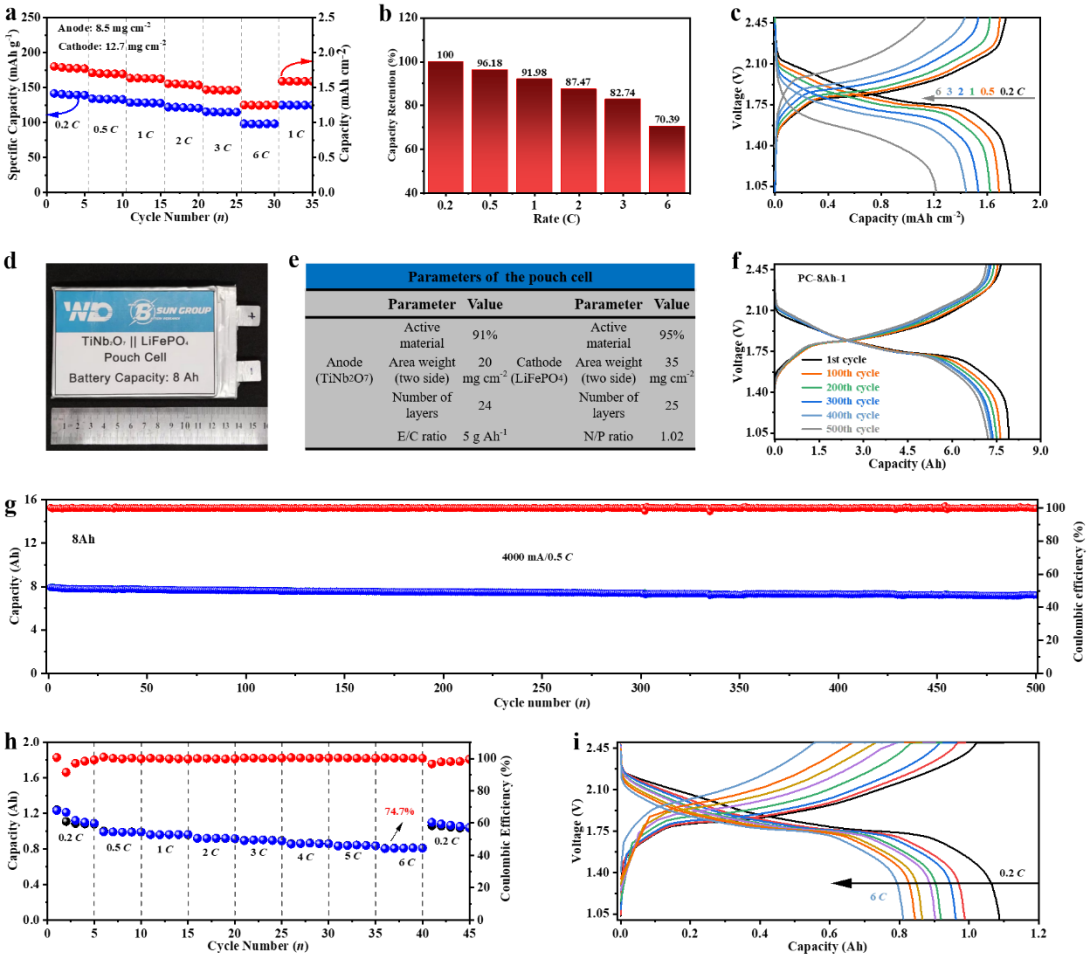

Figure 5. (a) The rate performance of $LiFePO_4||TiNb_2O_7$ full cell, (b) the corresponding capacity retention ratio, and (c) voltage-capacity plots of this full cell at different rates. (d) Optical photograph of the as-fabricated 8Ah-level $LiFePO_4||TiNb_2O_7$ pouch cells and (e) the corresponding parameters. (f) The voltage-capacity plots of this pouch cell at different cycles under a current density of 4000 mA. (g) The cyclability of this $LiFePO_4||TiNb_2O_7$ pouch cell under a current density of 4000 mA. (h) The rate performance of 1Ah-level $LiFePO_4||TiNb_2O_7$ pouch cell from 0.2 to 6 *C* and (i) the corresponding charge and discharge curves.

Conclusion

This paper investigated the relationship between electrochemical performances and electrode microstructures including porosity and electrode compaction, via experiments and theoretical modeling. Fundamental insights into the effect of electrode microstructure on electrochemical performance were provided, including rate capability, volumetric capacity, and materials utilization. Although lower porosity could shorten the ion and electron diffusion distance by decreasing electrode thickness, it would also result in narrower ion diffusion pathways and an increase in ion diffusion resistance. A paradigm of calendaring-driven

electrode microstructure was provided for balanced battery energy density and power density via employing a Wadsley-Roth phase $TiNb_2O_7$ anode. An optimized $TiNb_2O_7$ electrode with a high compaction density of ~2.5 g cm^{-3} and high mass loading of 8.5 mg cm^{-2} displayed the highest specific charge capacity of 271.3 mAh g^{-1} and high capacity retention (materials utilization) of 94.6% at 0.5 *C*, and 72.2% at 3 *C* in coin-type half cell configuration. Also, high capacity retention of 70.4% was realized in coin-type full cell configuration at 6 *C*. Furthermore, ~8 Ah level pouch full cells were fabricated and exhibited a high capacity retention of 91.1% for 500 cycles at 0.5 *C*. This study deepens our understanding on the dependence of electrochemical performance on the dual variation of compaction density and porosity and thus, provides insights into electrode microstructure regulation for optimized electrochemical performance to meet various applications.

Supporting Information

Supporting Information is available from the Wiley Online Library or from the author.

Acknowledgements

This work is financially supported by National Natural Science Foundation of China (No. 52072137). Siying Zhu was acknowledeged for data collation and schematic drawing. The Analytical and Testing Center of Huazhong University of Science and Technology was acknowledged for providing the facilities for materials characterization. Z.W.S. acknowledges the Singapore National Research Foundation (NRF-NRFF2017-04) and the Agency for Science, Technology and Research (Central Research Fund Award).

Conflict of Interest

The authors declare no conflict of interest.

References

[1] L. F. Zhao, Z. Hu, W. H. Lai, Y. Tao, J. Peng, Z. C. Miao, Y. X. Wang, S. L. Chou, H. K. Liu, S. X. Dou, *Adv. Energy Mater*. **2021**, *11*, 2002704.

[2] G. L. Zhu, C. Z. Zhao, J. Q. Huang, C. He, J. Zhang, S. Chen, L. Xu, H. Yuan, Q. Zhang, *Small* **2019**, *15*, 1805389.

[3] S. Li, K. Wang, G. Zhang, S. Li, Y. Xu, X. Zhang, X. Zhang, S. Zheng, X. Sun, Y. Ma, *Adv. Funct. Mater.* **2022**, 2200796.

[4] J. Billaud, F. Bouville, T. Magrini, C. Villevieille, A. R. Studart, *Nat. Energy* **2016**, *1*, 16097.

[5] S. Huang, Z. Li, B. Wang, J. Zhang, Z. Peng, R. Qi, J. Wang, Y. Zhao, *Adv. Funct. Mater*. **2018**, *28*, 1706294.

[6] S. Fu, X. Yu, Q. Wu, X. Yang, Z. Liu, X. Li, S. He, D. Wang, Y. Li, S. Tong, M. Wu, *Adv. Energy Mater*. **2021**, *11*, 2003270.

[7] S. Deng, H. Zhu, B. Liu, L. Yang, X. Wang, S. Shen, Y. Zhang, J. Wang, C. Ai, Y. Ren, Q. Liu, S. Lin, Y. Lu, G. Pan, J. Wu, X. Xia, J. Tu, *Adv. Funct. Mater*. **2020**, *30*, 2002665.

[8] X. Zhang, S. Deng, Y. Zeng, M. Yu, Y. Zhong, X. Xia, Y. Tong, X. Lu, *Adv. Funct. Mater*. **2018**, *28*, 1805618.

[9] Y. Y. Liu, Y. Y. Zhu, Y. Cui, *Nat. Energy* **2019**, *4*, 540.

[10] N. Kim, S. Chae, J. Ma, M. Ko, *Nat. Commun.* **2017**, *8*, 812.

[11] R. J. Cava, D. W. Murphy, S. M. Zahurak, *J. Electrochem. Soc.* **1983**, *130*, 2345.

[12] Y. Yang, J. Zhao, A*dv. Sci*. **2021**, *8*, 2004855.

[13] W. Wu, M. Liu, Y. Pei, W. Li, W. Lin, Q. Huang, M. Wang,H. Yang, L. Deng, L. Yao, Z. Zheng, *Adv. Energy Mater*. **2022**, 2201130. (DOI: 10.1002/aenm.202201130)

[14] Y. Yang, J. Huang, Z. Cao, Z. Lv, D.Wu, Z.Wen, W. Meng, J. Zeng, C. Chao Li, J. Zhao, *Adv. Sci*.**2022**, *9*, 2104530.

[15] G. Liang, V. K. Peterson, Z. Wu, S. Zhang, J. Hao, C.-Z. Lu, C.-H. Chuang, J.-F. Lee, J. Liu, G. Leniec, S. M. Kaczmarek, A. M. D'Angelo, B. Johannessen, L. Thomsen, W. K. Pang, Z. Guo, *Adv.Mater*. **2021**, *33*, 2101413.

[16] Y. C. Yang, B. H. Qiao, X. M. Yang, L. B. Fang, C. C. Pan, W. X. Song, H. S. Hou, X. B. Ji, *Adv. Funct. Mater.* **2014**, *24*, 4349.

[17] M. M. Thackeray, K. Amine, *Nat. Energy* **2021**, *6*, 683.

[18] H. Zhang, L. Wang, H. Li, X. He, *ACS Energy Lett.* **2021**, *6*, 3719.

[19] H. G. Jung, M. W. Jang, J. Hassoun, Y. K. Sun, B. Scrosati, *Nat. Commun.* **2011**, *2*, 516.

[20] J. T. Han, Y. H. Huang, J.B. Goodenough, *Chem. Mater.* **2011**, *23*, 2027.

[21] J. T. Han, J.B. Goodenough, *Chem. Mater.* **2011**, *23*, 3404.
[22] X. Lu, Z. Jian, Z. Fang, L. Gu, Y. S. Hu, W. Chen, Z. Wang, L. Chen, *Energy Environ. Sci.* **2011**, *4*, 2638.
[23] K. J. Griffith, I. D. Seymour, M. A. Hope, M. M. Butala, L. K. Lamontagne, M. B. Preefer, C. P. Kocer, G. Henkelman, A. J. Morris, M. J. Cliffe, S. E. Dutton, C. P. Grey, *J. Am. Chem. Soc.* **2019**, *141*, 16706.
[24] J. Wu, P. Liu, Y. Hu, H. Li, *Energy Storage Sci. Technol.* **2016**, *5*, 443.
[25] T.Tian, L.-L. Lu, Y.-C. Yin, F.Li, T.-W. Zhang, Y.-H. Song, Y.-H. Tan, H.-B. Yao, *Adv. Funct. Mater.* **2021**, *31*, 2007419.
[26] X. Lu, S. R. Daemi, A. Bertei, M. D.R. Kok, K. B. O'Regan, L. Rasha, J. Park, G. Hinds, E. Kendrick, D. J.L. Brett, P. R. Shearing, *Joule* **2020**, *4*, 2746.
[27] A. Kwade, W. Haselrieder, R. Leithoff, A. Modlinger, F. Dietrich, K. Droeder, *Nat. Energy* **2018**, *3*, 290.
[28] G. Lenze, F. Roder, H. Bockholt, W. Haselrieder, A. Kwade, U. Krewer, *J. Electrochem. Soc*. **2017**, *164*, A1223.
[29] H. Zheng, L. Tan, G. Liu, X. Song, V. S. Battaglia, *J. Power Sources* **2012**, *208*, 52.
[30] Z. Du, D. L. Wood, C. Daniel, S. Kalnaus, J. Li, *J. Appl. Electrochem.* **2017**, *47*, 405.
[31] M. Xu, B. Reichman, X. Wang, *Energy* **2019**, *186*, 115864.
[32] T. Danner, M. Singh, S. Hein, J. Kaiser, H. Hahn, A. Latz, *J. Power Sources* **2016**, *334*, 191.
[33] R. Zhao, J. Liu, J. Gu, *Appl. Energy* **2015**, *139*, 220.
[34] H. Zhenga, J. Li, X. Song, G. Liu, V. S. Battaglia, *Electrochim. Acta*, **2012**, *71*, 258.
[35] A. Davoodabadi, J. Li, Y. Liang, D. L. Wood, T. J. Singler, C.Jin, *J. Power Sources* **2019**, *424*,193.
[36] A. Davoodabadi, J. Li, Y. Liang, R. Wang, H. Zhou, D. L. Wood, T. J. Singler, C. Jin, *J. Electrochem. Soc.* **2018**, *165*, A2493.
[37] W. Haselrieder, S. Ivanov, D. K. Christen, H. Bockholt, A. Kwade, *ECS Trans*. **2013**, *50*, 59.
[38] Y. Sheng, C. R. Fell, Y. K. Son, B. M. Metz, J. Jiang, B. C. Church, *Front. Energy Res*. **2014**, *2*, 56.
[39] C. Meyer, M. Kosfeld, W. Haselrieder, A. Kwade, *J. Energy Storage* **2018**, *18*, 371.
[40] C. Meyer, H. Bockholt, W. Haselrieder, A. Kwade, *Journal of Materials Processing Tech.* **2017**, *249*, 172.

[41] Z. Yao, X. Xia, Y. Zhang, D. Xie, C. Ai, S. Lin, Y. Wang, S. Deng, S. Shen, X. Wang, Y. Yue, J. Tu, *Nano Energy* **2018**, *54*, 304.

[42] M. Doyle, T. F. Fuller, J. Newman, *J. Electrochem. Soc.* **1993**, *140*, 1526.

A paradigm of calendaring-driven electrode microstructure for balanced battery energy density and power density

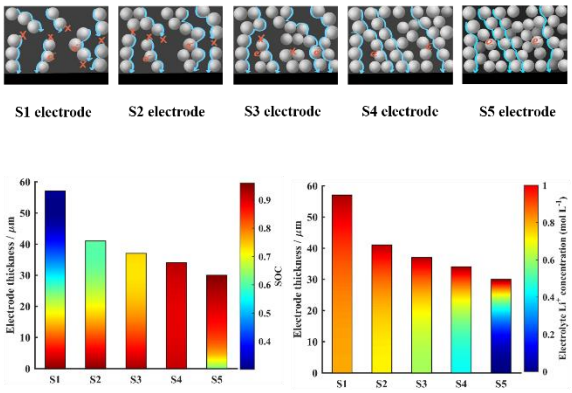

In this article, the dependence of electrochemical performance on dual variation of electrode compaction density and porosity has been studied *via* experiments and theoretical modeling. A paradigm of calendaring-driven electrode microstructure was realized for balanced battery energy density and power density using a Wadsley-Roth phase $TiNb_2O_7$ anode as an example.

Supporting Information

A paradigm of calendaring-driven electrode microstructure for balanced battery energy density and power density

Renming Zhan, Dongsheng Ren, Shiyu Liu, Zhengxu Chen, Xuerui Liu, Wenyu Wang, Lin Fu, Xiancheng Wang, Shuibin Tu, Yangtao Ou, Hanlong Ge, Andrew Jun Yao Wong, Zhi Wei Seh, Li Wang, and Yongming Sun*

1. Experimental Section

***Material preparation*:** $TiNb_2O_7$ was fabricated by a one-step solid-state reaction using TiO_2 and Nb_2O_5 as precursors. Stoichiometric amounts of the precursors were fully mixed, and annealing at 1100 ℃ for 12 h in a muffle furnace.

***Electrodes preparation*:** $TiNb_2O_7$ electrodes were fabricated using doctor blade approach, which consisted of 90 wt% active material, 7 wt% super P conductive additive, and 3 wt% hybrid binder (carboxy methylcellulose: styrene-butadiene rubber = 1:1 in weight). For coin-cell evaluation, the $TiNb_2O_7$ electrodes with the same mass loading (~8.5 mg cm^{-2}) were coated onto a single side of the current collector. Electrodes with different compaction densities and porosities (S1-S5 electrodes) were produced using a rolling machine with different slit distances. For pouch cell measurement, $TiNb_2O_7$ electrode was coated on both sides of the current collector with a total mass loading of ~20 mg cm^{-2}.

***Material characterization*:** The phase information of materials were collected by X-ray diffraction (XRD, Empyrean). Morphology of the materials and electrodes was investigated by Nova NanoSEM 450 field-emission scanning electron microscope (SEM).

***Electrochemical analysis*:** CR2032 coin-type cells and pouch cells were assembled in an Ar-filled Mikrouna glovebox (Shanghai, China) using polypropylene membrane as the separator, and 1 M $LiPF_6$ in a mixed solvent of ethylene carbonate, dimethyl Carbonate, ethyl methyl carbonate (1:1:1 in volume) as the electrolyte. The charging/discharging measurements were

carried out at room temperature on LAND CT-3001A and LAND CT-3002B battery testers (Wuhan, China), respectively. The cut-off voltage ranges were 1.0-3.0 V for $TiNb_2O_7$||Li half cells and 1.0-2.5 V for $LiFePO_4$||$TiNb_2O_7$ full cells, respectively. BioLogic VMP-300 electrochemical workstation was employed to conduct cyclic voltammogram (CV) and electrochemical impedance spectroscopy (EIS) measurements. Various scan rates including 0.1, 0.2, 0.4, 0.8 and 1 mV s^{-1} were adopted for CV measurement. The frequency range for EIS measurement was 100 mHz -100 KHz with an amplitude of 10 mV. The electrode resistivity and conductivity of S1-S5 electordes were measured by RTS-9 four-probe instrument (4Probes Tech Ltd. Guangzhou, China).

***Calculation of the volumetric capacities for electrodes*:** The theoretical volumetric capacity (C_v) of electrode active materials was caculated as $C_v=C_g*\rho$,[1] where C_g was gravimetric capacity and ρ was true density.

***Simulation of the electrochemical performance for electrodes*:** An electrochemical model was bulit in COMSOL Multiphysics (ver5.4) based on Newman's P2D model to simulate the electrochemical performance of $TiNb_2O_7$ electrodes (S1-S5) with different compaction densities. The governing equations were listed in Table S3, and the physical variables were presented Table S4. In the electrochemical model, the $TiNb_2O_7$ was defined as the working electrode with the thickness of L_n, lithium anode was the counter electrode and modeled as a large lithium reservoir with a constant potential of 0 V, and a porous separator with a thickness of L_{sep} was placed between the $TiNb_2O_7$ electrode and lithium anode. The battery output voltage was calculated by the solid phase potential in the interface between $TiNb_2O_7$ electrode and current collector, as in Eq. (1). The charge balance in the solid phase of the $TiNb_2O_7$ electrode followed the Ohm's law, as in Eq. (2), and the charge balance in the electrolyte phase was influenced by the Ohm's law and migration of the cation and anions, as in presented in Eq. (3). The mass balance in the solid phase was controlled by the diffusion of the Li^+ inside the $TiNb_2O_7$ electrode particle, and the governing equation in Eq. (4). The Li^+ concentration in the electrolyte phase was also affected by the diffusion and migration processes, while the convection process was neglected in the model, as showed in Eq. (5). The Li^+ flux in the interface between $TiNb_2O_7$ electrode and electrolyte was determined by the reaction kinetics equation (the Butler-Volmer formula in Eq.(6)), with the exchange current density, overpotential and open circuit potential in Eq. (7)~(9). The electrochemical model was then established in COMSOL Multiphysics (ver5.4) using its *Batteries and Fuel Cells* module, with the related physio-electrochemical parameters used in the electrochemical model listed in Table S5. Further details of the establishment and sloving process of the electrochemical model can

be accessed in the COMSOL Multiphysics Application Library (https://www.comsol.com/models/?q=battery&sort=relevance).

2. Supplementary Figures

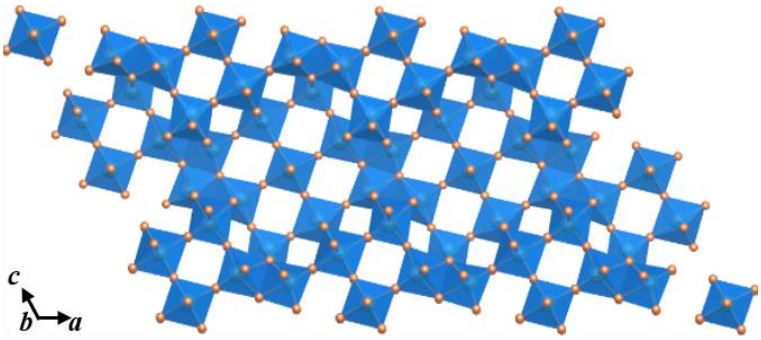

Figure S1. Crystal structure of $TiNb_2O_7$.

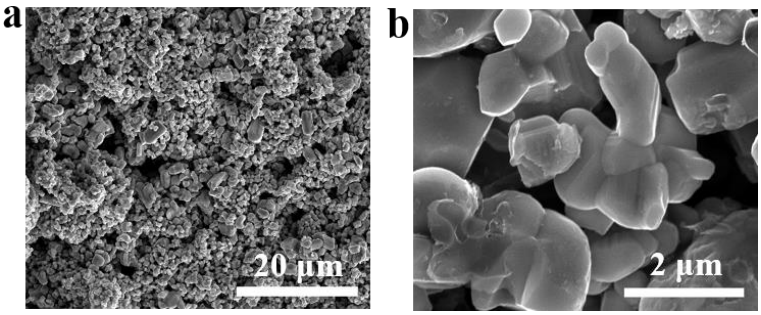

Figure S2. SEM images of $TiNb_2O_7$.

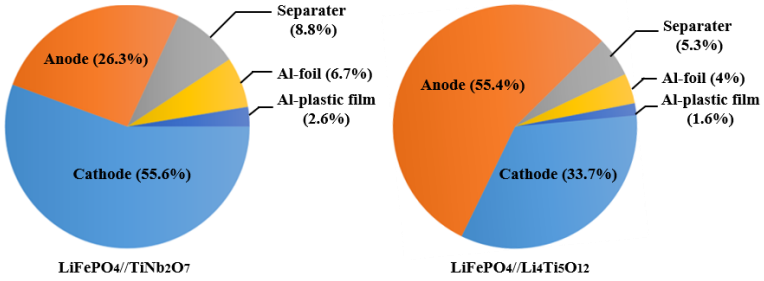

Figure S3 Volume fractions of different components in10 Ah-level $LiFePO_4$‖$TiNb_2O_7$ and $LiFePO_4$‖$Li_4Ti_5O_{12}$ pouch cells, respectively.

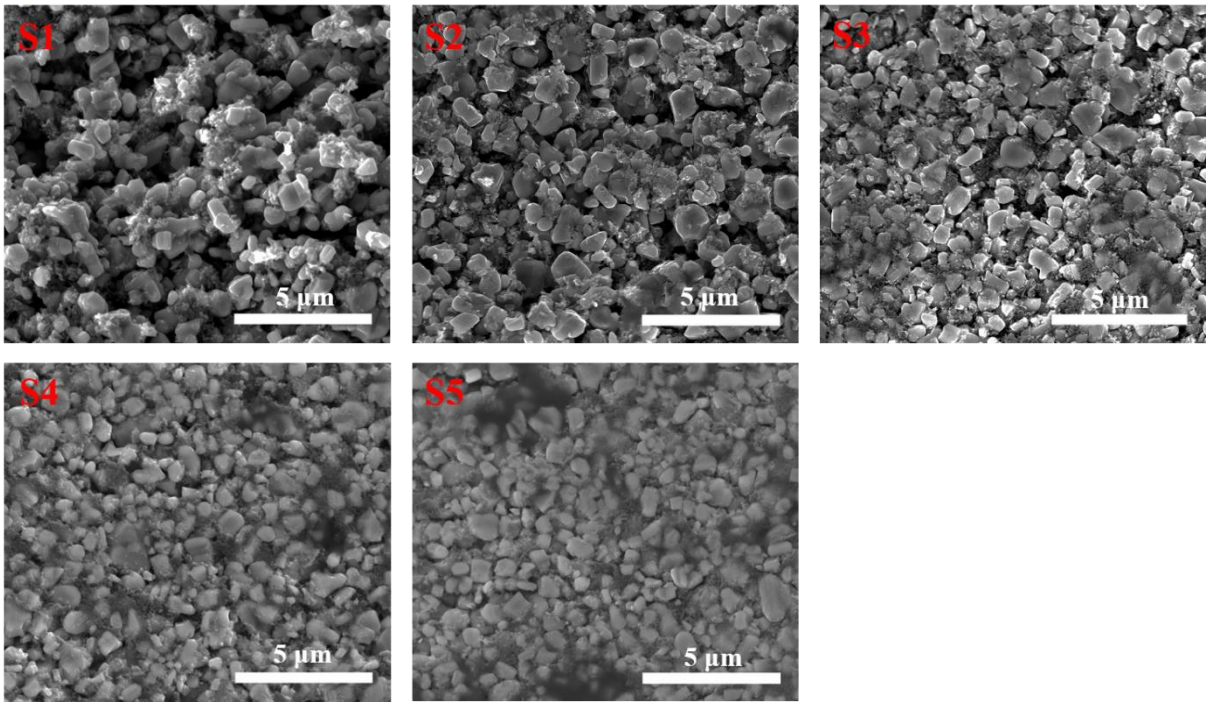

Figure S4. Cross-section SEM images of $TiNb_2O_7$ electrodes with different compaction densities (S1-S5).

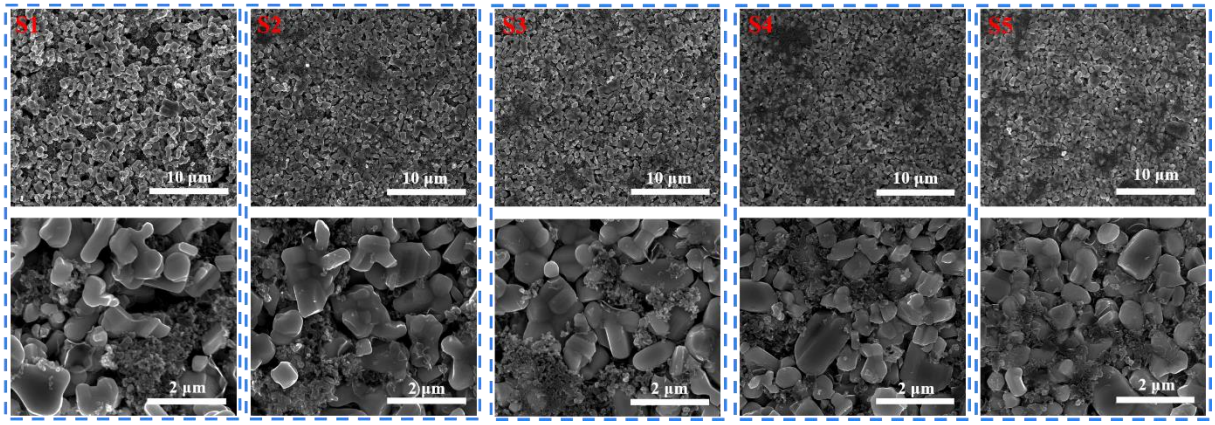

Figure S5. Top-view SEM images of $TiNb_2O_7$ electrodes with different compaction densities (S1-S5).

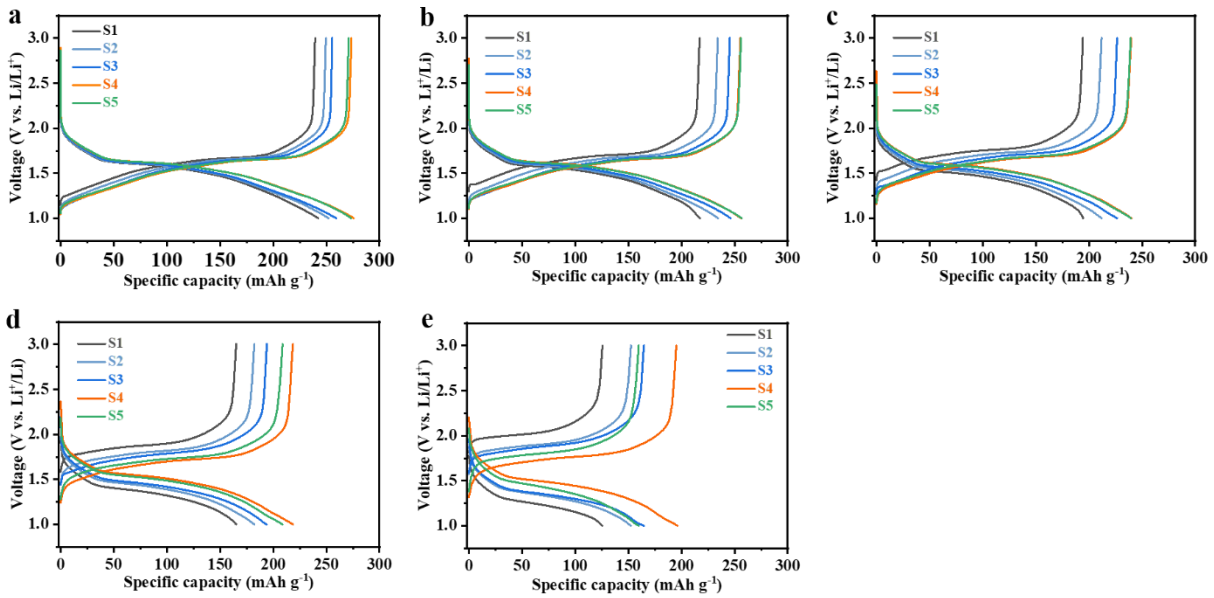

Figure S6. (a-e) Voltage-capacity plots of $TiNb_2O_7$ electrodes with different compaction densities at different *C*-rates (0.2, 0.5, 1, 2 and 3 *C*).

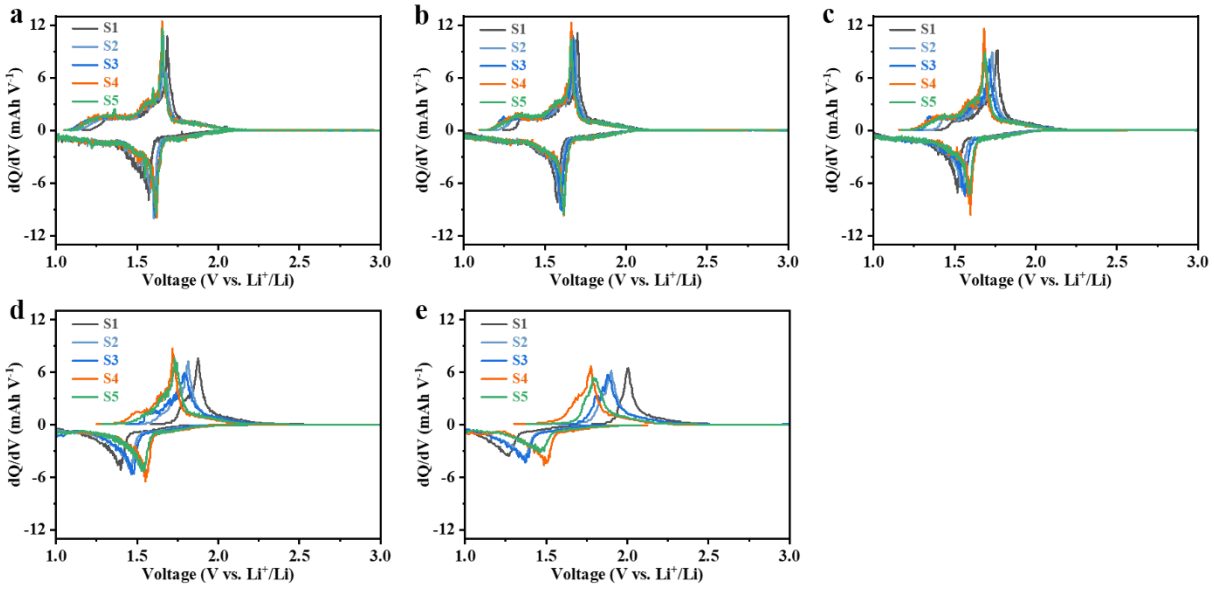

Figure S7. (a-e) dQ/dV profiles of $TiNb_2O_7$ electrodes with different compaction densities at different *C*-rates (0.2, 0.5, 1, 2 and 3 *C*).

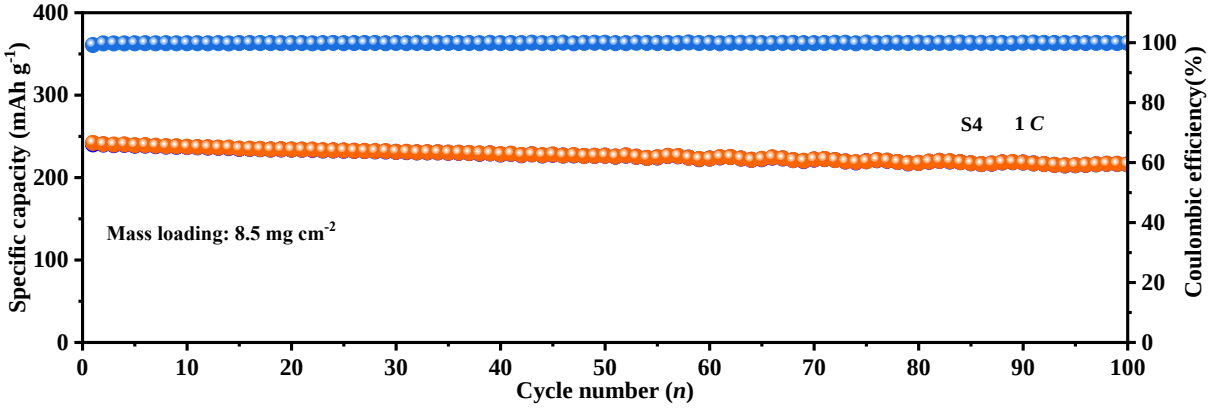

Figure S8. The cycling performance of the S4 electrode at 1 *C*.

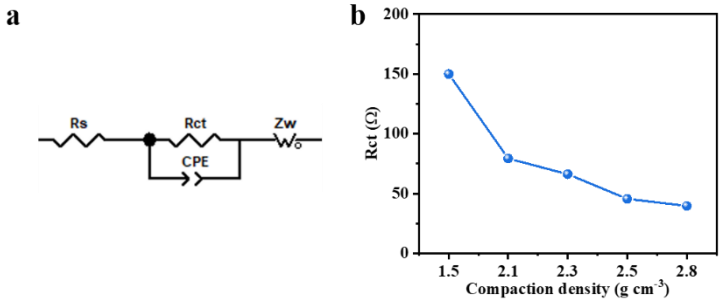

Figure S9. (a) Equivalent electrical circuit for the electrochemical impedance spectra of the S1-S5 electrodes and (b, c) the corresponding electrochemical impedance spectra fitting results and values of the S1-S5 electrodes at same state of charge, respectively.

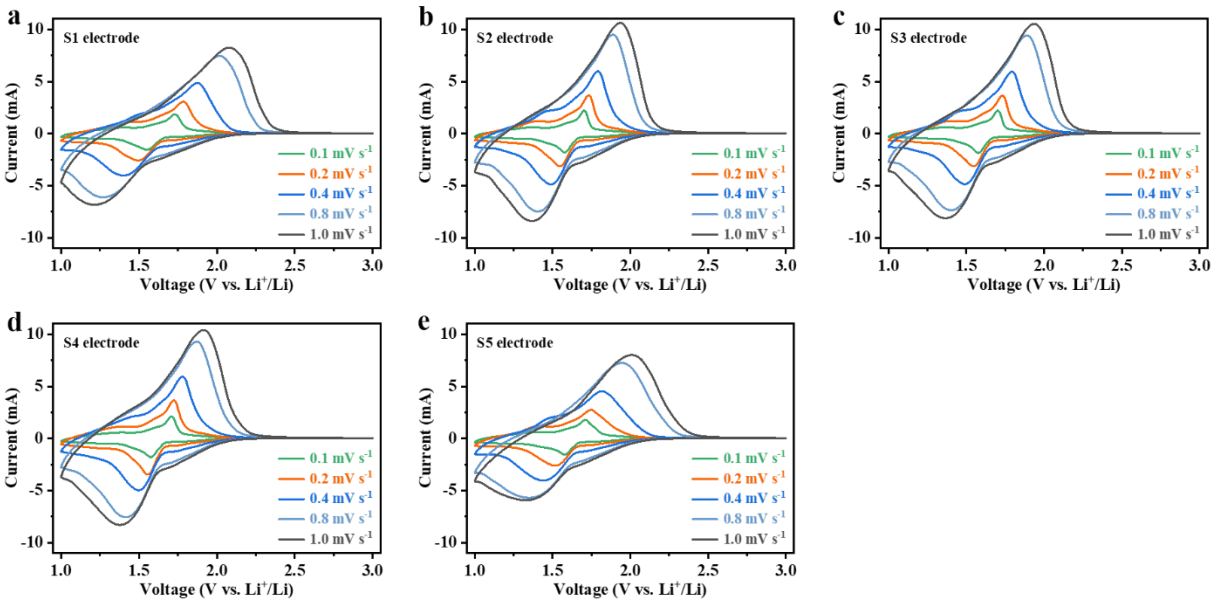

Figure S10. (a-e) CV profiles of $TiNb_2O_7$ electrodes with different compaction densities at different scanning rates.

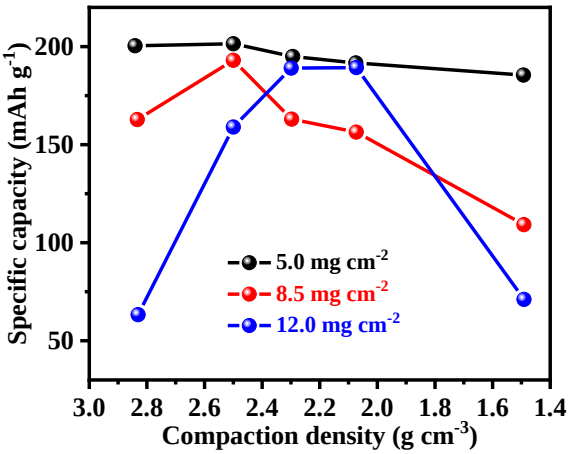

Figure S11 The relationship of active materials utilization of S1-S5 electrodes with different mass loadings at 3 *C*.

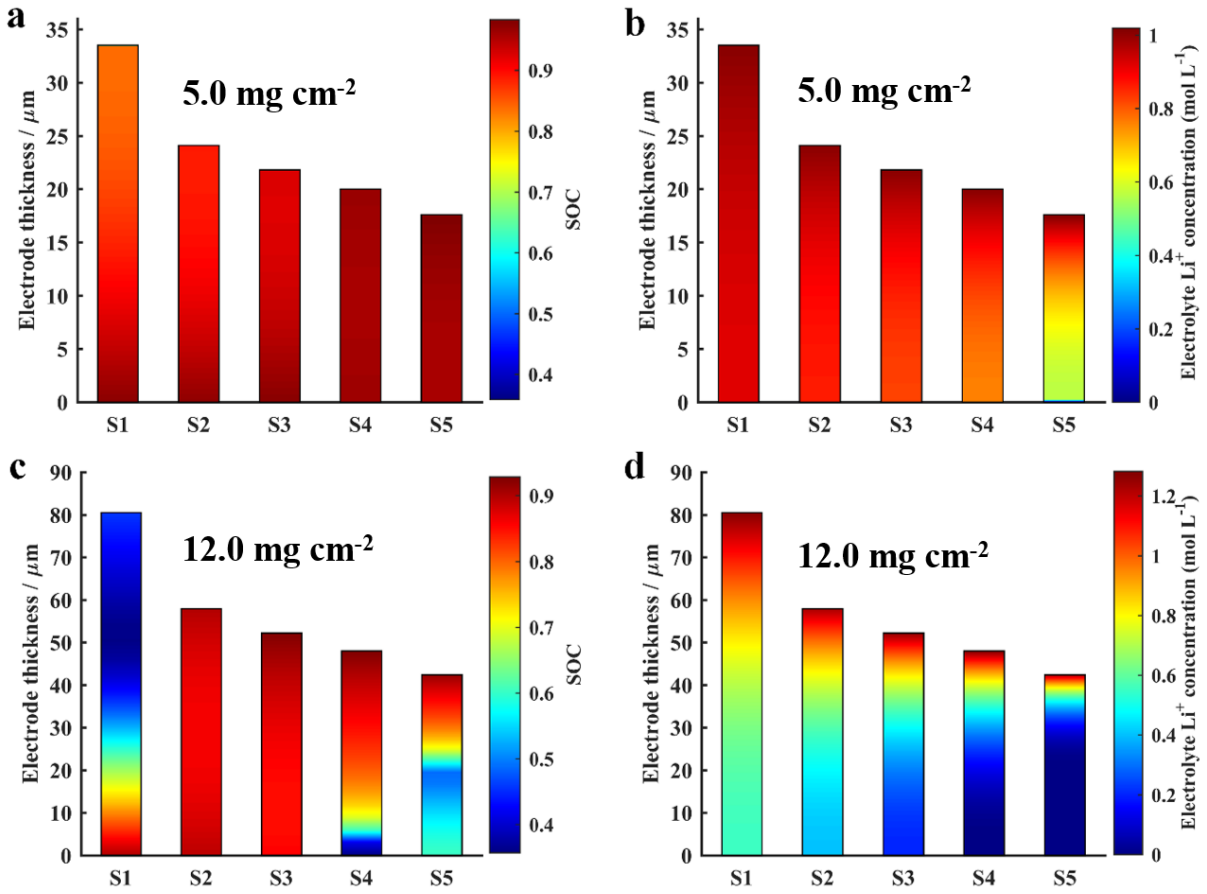

Figure S12 Distribution of Li^+ concentration in (a,c) $TiNb_2O_7$ electrodes and (b,d) electrolytes at the end of charged state at 3 *C*. The mass loadings for $TiNb_2O_7$ electrodes in (a,b) and (c,d) were 5.0 and 12.0 mg cm^{-2}, respectively.

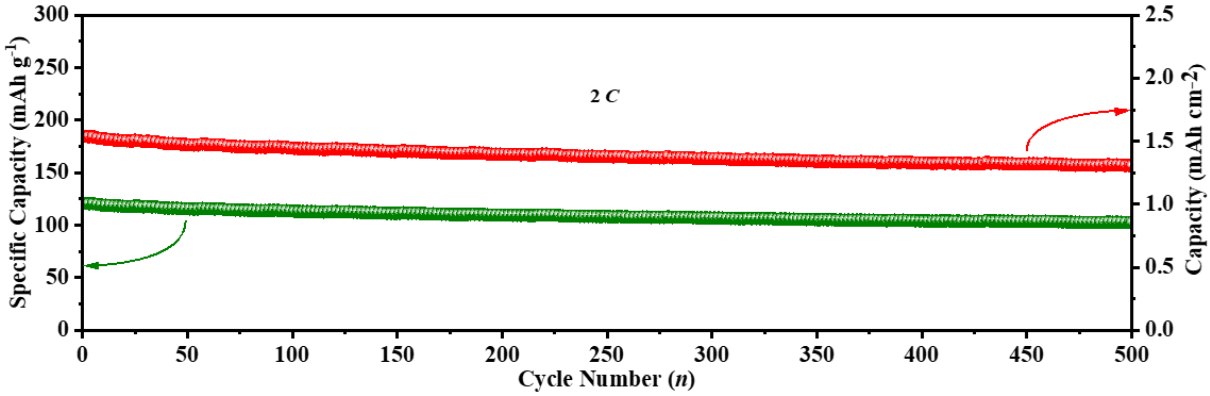

Figure S13. Cycling stability of $TiNb_2O_7$‖$LiFePO_4$ full battery at 2 *C*.

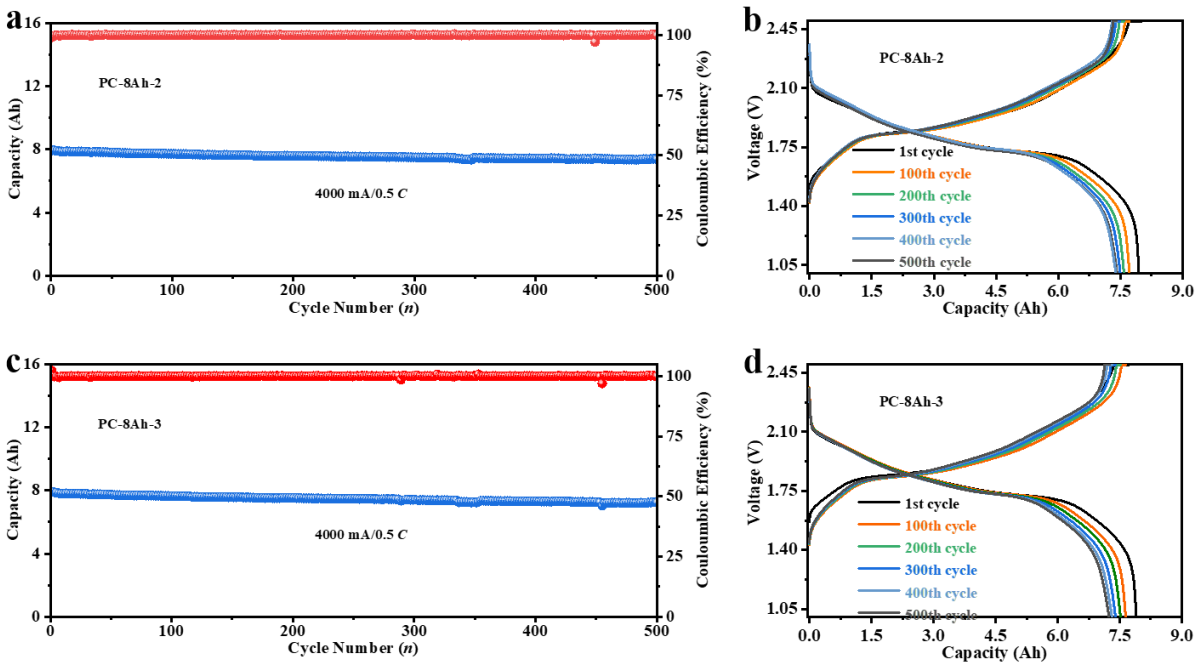

Figure S14. (a, c) The cycling performance of two 8Ah-level pouch cells at 4000 mA, and (b, d) the voltage-capacity plots for different cycles (corresponding to Figure S12a, 12c, respectively).

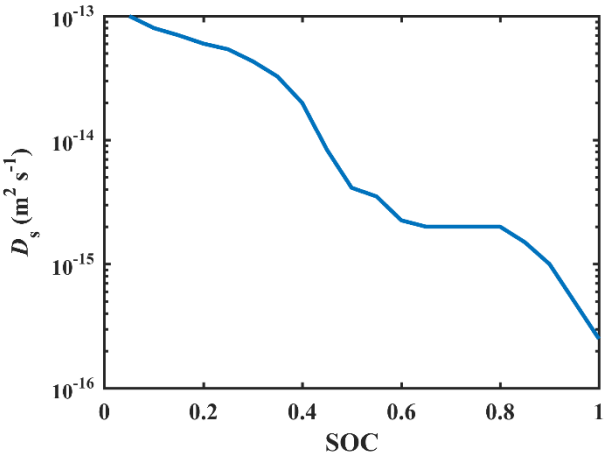

Figure S15. Variations of D_s with the SOC of the $TiNb_2O_7$ electrode. The value of D_s was determined manually during the simulation to fit the experimental data.

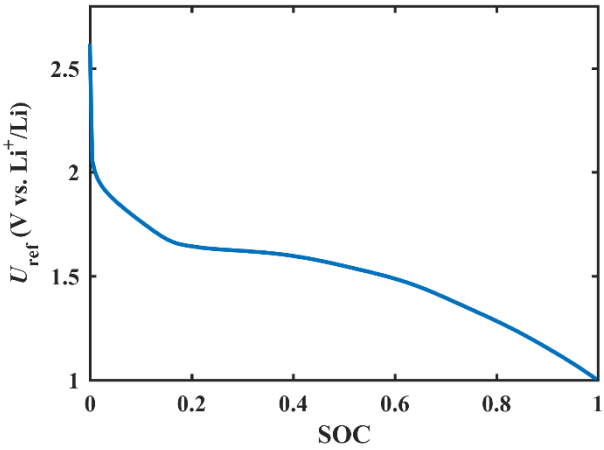

Figure S16. Variations of Uref with the SOC of the $TiNb_2O_7$ electrode. The Uref was obtained from the 0.2 *C* charging test of the $TiNb_2O_7$ electrode.

3. Supplementary Tables

Table S1. The calculated parameters of 10 Ah-level$LiFePO_4$‖$TiNb_2O_7$pouch cell.

	Parameter	Value		Parameter	Value
Anode ($TiNb_2O_7$)	Active material loading	91 Wt%	Cathode ($LiFePO_4$)	Active material loading	95 Wt%
	Area weight (double side)	20 mg cm^{-2}		Area weight (double side)	35 mg cm^{-2}
	Number of layers	33		Number of layers	32
	compaction density	2.8 g cm^{-3}		compaction density	2.3 g cm^{-3}
	Al foil	9μm		Separater	12μm
	Al-plastic film	113μm		Pouch cell size	80.5*85 mm

Table S2. The calculated parameters of 10 Ah-level‖$LiFePO_4$||$Li_4Ti_5O_{12}$pouch cell.

	Parameter	Value		Parameter	Value
Anode ($Li_4Ti_5O_{12}$)	Active material loading	91 Wt%	Cathode ($LiFePO_4$)	Active material loading	95 Wt%
	Area weight (double side)	32.5 mg cm^{-2}		Area weight (double side)	35 mg cm^{-2}
	Number of layers	33		Number of layers	32
	compaction density	1.3 g cm^{-3}		compaction density	2.3 g cm^{-3}
	Al foil	9μm		Separater	12μm
	Al-plastic film	113μm		Pouch cell size	80.5*85 mm

Table S3. The governing equations of the electrochemical model.

	Equation expressions		Boundary conditions
Output voltage	$V=\phi_s\big\vert_{x=L_n+L_{sep}}$	(1)	
Charge balance equation, solid phase	$\frac{\partial}{\partial x}\left(\sigma_s^{eff}\frac{\partial}{\partial x}\phi_s\right)-a_sFj=0$	(2)	$-\sigma_s^{eff}\frac{\partial}{\partial x}\phi_s\big\vert_{x=L_n+L_{sep}}=i_{app}$ $\frac{\partial}{\partial x}\phi_s\big\vert_{x=L_n+L_{sep}}=0$
Charge balance equation, electrolyte phase	$\frac{\partial}{\partial x}\left(\kappa_e^{eff}\frac{\partial}{\partial x}\phi_e\right)+\frac{2RT(t_+-1)}{F}\frac{\partial}{\partial x}\left(\kappa_e^{eff}\frac{\partial}{\partial x}\ln c_e\right)+a_sFj=0$	(3)	$\frac{\partial}{\partial x}\phi_e\big\vert_{x=L_n+L_{sep}}=0$
Mass balance equation, solid phase	$\frac{\partial c_s}{\partial t}-\frac{D_s}{r^2}\frac{\partial}{\partial r}\left(r^2\frac{\partial c_s}{\partial r}\right)=0$	(4)	$D_s\frac{\partial c_s}{\partial r}\big\vert_{r=0}=0$, $D_s\frac{\partial c_s}{\partial r}\big\vert_{r=R_s}=-j$
Mass balance equation, electrolyte phase	$\frac{\partial}{\partial t}(\varepsilon_e c_e)=\frac{\partial}{\partial x}\left(D_e^{eff}\frac{\partial}{\partial x}c_e\right)+(1-t_+)a_sj$	(5)	$\frac{\partial}{\partial x}c_e\big\vert_{x=0}=i_{app}$ $\frac{\partial}{\partial x}c_e\big\vert_{x=L_n+L_{sep}}=0$
Electrochemical reaction kinetics equation	$j=i_0\cdot\left[\exp\left(\frac{\alpha_aF\eta}{RT}\right)-\exp\left(\frac{-\alpha_cF\eta}{RT}\right)\right]$	(6)	
Exchange current density	$i_0=k\cdot c_e^{\alpha_a}(c_{s,max}-c_{s,surf})^{\alpha_a}c_{s,surf}^{\alpha_c}$	(7)	
Reaction overpotential	$\eta=\phi_s-\phi_e-U$	(8)	
Open circuit potential	$U=U_{ref}(x)$	(9)	

Table S4. The variables in the electrochemical model.

Symbol	Description	Unit
ϕ_s	Electrical potential in the solid phase	V
ϕ_e	Electrical potential in the electrolyte phase	V
c_s	Li^+ concentration in the solid phase	$mol\cdot m^{-3}$
c_e	Li^+ concentration in the electrolyte	$mol\cdot m^{-3}$
j	Current density in the solid-electrolyte interface	$mol\cdot m^{-2}\cdot s^{-1}$
T	Battery temperature	K

Table S5. The parameters used in the electrochemical model.

Symbol	Parameter	Unit	Value
F	Faraday constant	$C \cdot mol^{-1}$	96487
R	Ideal gas constant	$J \cdot mol^{-1} \cdot K^{-1}$	8.314
T_{ref}	Reference temperature	K	298.15
L	Thickness	μm	57 /41/37/34/30
R_n	Particle radius	μm	3
ε_s	Volume fraction of the active particle	1	0.31/0.43/0.48/0.52/0.59
ε_e	Volume fraction of the electrolyte phase	1	0.61/0.46/0.41/0.36/0.28
a_s	Specific interfacial area	m^{-1}	$3\varepsilon_s/R_s$
σ_s^{eff}	Effective electrical conductivity in the solid phase	$mS \cdot m^{-1}$	3.5/3.6/4.5/16.2/32.4
κ_e	Electrical conductivity in the electrolyte phase	$S \cdot m^{-1}$	[2]
κ_e^{eff}	Effective electrical conductivity in the electrolyte phase	$S \cdot m^{-1}$	$\varepsilon_e^{2.75}\sigma_e$
$c_{e,0}$	Initial value of Li^+ concentration in the electrolyte phase	$mol \cdot m^{-3}$	1000[a]
$c_{s,max}$	Maximum solid phase Li^+ concentration	$mol \cdot m^{-3}$	45906.7
D_s	Solid phase diffusion coefficient	$m^2 \cdot s^{-1}$	Figure S15
D_e	Electrolyte phase diffusion coefficient	$m^2 \cdot s^{-1}$	[2]
D_e^{eff}	Effective electrolyte phase diffusion coefficient	$m^2 \cdot s^{-1}$	$\varepsilon_e^{2.75}D_e$
t_+	Transference number	1	[2]
α_a, α_c	Transfer coefficients of lithium intercalation reaction	1	0.5, 0.5
k	Reaction rate constant of lithium intercalation reaction at T_{ref}	$m^{2.5} \cdot mol^{-0.5} \cdot s^{-1}$	2.5×10^{-9}
U_{ref}	Open circuit potential	V	Figure S16

References

[1] B. Wang, X. Li, T. Qiu, B. Luo, J. Ning, J. Li, X. Zhang, M. Liang, L. Zhi, *Nano Lett.* **2013**, *13*, 5578.

[2] L. O. Valøen, J. N. Reimers, *J. Electrochem. Soc.* **2005**, *152*, A882.